Title

Elemental Topological Dirac Semimetal: α-Sn on InSb(111)

Journal

Physical Review Letters, 118(14)

ISSN

0031-9007

Authors

Xu, Cai-Zhi

Chan, Yang-Hao

Chen, Yige

et al.

Publication Date

2017-04-07

DOI

10.1103/physrevlett.118.146402

Peer reviewed

Elemental topological Dirac semimetal: α-Sn on InSb(111)

Cai-Zhi Xu[1,2,3], Yang-Hao Chan[4], Yige Chen[5], Peng Chen[1,2,3], Xiao-Xiong Wang[1,2,6], Catherine Dejoie[7], Man-Hong Wong[1,2], Hyejin Ryu[3], Joseph Andrew Hlevyack[1,2], Hae-Young Kee[5], Nobumichi Tamura[3], Mei-Yin Chou[4,8,9], Zahid Hussain[3], Sung-Kwan Mo[3] * and Tai-Chang Chiang[1,2,9] *

[1]Department of Physics, University of Illinois at Urbana-Champaign, Urbana, Illinois 61801, USA

[2]Frederick Seitz Materials Research Laboratory, University of Illinois at Urbana-Champaign, Urbana, Illinois 61801, USA

[3]Advanced Light Source, Lawrence Berkeley National Laboratory, Berkeley, California 94720, USA

[4]Institute of Atomic and Molecular Sciences, Academia Sinica, Taipei 10617, Taiwan

[5]Department of Physics, University of Toronto, Toronto, Ontario M5S 1A7, Canada

[6]College of Science, Nanjing University of Science and Technology, Nanjing 210094, China

[7]Structure of Materials Group, ESRF-The European Synchrotron CS40220, 38043 Grenoble Cedex 9, France

[8]School of Physics, Georgia Institute of Technology, Atlanta, Georgia 30332, USA

[9]Department of Physics, National Taiwan University, Taipei 10617, Taiwan

** Correspondence and requests for materials should be addressed to S.-K.M. (email: SKMo@lbl.gov) or T.-C.C. (email: tcchiang@illinois.edu).*

Three-dimensional (3D) topological Dirac semimetals (TDSs) are rare but important as a versatile platform for exploring exotic electronic properties and topological phase transitions[1–5]. A quintessential feature of TDSs are 3D Dirac fermions associated with bulk electronic states near the Fermi level[3–9]. Using angle-resolved photoemission spectroscopy (ARPES), we have observed such bulk Dirac cones in epitaxially-grown α-Sn films on InSb(111), the first such TDS system realized in an elemental form. First-principles calculations confirm that epitaxial strain is key to the formation of the TDS phase. A phase diagram is established that connects the 3D TDS phase through a singular point of a zero-gap semimetal phase to a topological insulator (TI) phase. The nature of the Dirac cone crosses over from 3D to 2D as the film thickness is reduced.

Recent years have witnessed an ever-growing interest in materials that host Dirac fermions; examples include graphene, TIs and Dirac semimetals[1,5,10–12]. In 3D TDSs, the bulk valence band (VB) and conduction band (CB) touch at multiple discrete points in the bulk Brillouin zone to form Dirac points, near which the dispersion relations are linear in all three momentum directions[2,5]. Furthermore, these materials can support nontrivial surface states[3,4,9,13]. The unusual electronic structure leads to extraordinary physical properties including giant linear magnetoresistance[14–17], ultrahigh carrier mobility[7,17], chiral anomaly[18–20] and quantum oscillations[21]. Theoretically, TDSs can be driven by symmetry breaking into TIs and Weyl semimetals[3,5,18,22]; thus, these materials are excellent parent compounds for realizing other exotic electronic phases. They also provide an excellent test ground for studies of topological phase transitions. TDSs are rare, however, because the topological conditions on the electronic structure are generally hard to satisfy. Thus far, Na_3Bi and Cd_3As_2 are the only two known cases[5–9,23]. Herein, we show that α-Sn, a simple elemental material, can be made into a TDS under a suitable strain achieved experimentally through molecular beam epitaxial (MBE) growth of Sn thin films on InSb(111). While bulk α-Sn, with the diamond lattice structure, is stable only below 13 °C, thin films of α-Sn grown on InSb can be stable up to ~170 °C[24]. The lattices of α-Sn and InSb are nearly matched, but a slight mismatch results in an in-plane compressive strain of 0.14% for the α-Sn overlayer[25,26].

The crystal structure of (111)-oriented α-Sn films is shown in Fig. 1a. It consists of a stack of bilayers (BLs). Each BL is a stanene, which resembles graphene but is buckled with the two hexagonal sublattices at different heights[27,28]. Fig. 1b shows the hexagonal prismatic bulk Brillouin zone and the (111)-projected surface Brillouin zone. A reflection-high-energy-electron-diffraction (RHEED) pattern of a 30-BL α-Sn(111) film grown on InSb(111) (Fig. 1c) demonstrates a good film quality. The pattern also reveals a 3×3 reconstruction, which is known to exist on the α-Sn(111) face[24]. Fig. 1d shows RHEED intensity as a function of deposition time. The periodic oscillatory behavior indicates a layer-by-layer growth mode and permits precise determination of the film thickness. Fig. 1e shows a photoemission spectrum of the 30-BL film; it is dominated by the Sn 4*d* core level doublet. No signals from the substrate In or Sb are detected; thus the film is continuous with no pin holes or cracks. The strain in the 30-BL film is measured by X-ray diffraction using the $sin^2\psi$ technique (see details in Methods). The results, shown in Fig. 1f, yield an in-plane compressive strain $\varepsilon_{\parallel}$ = (-0.14 ± 0.03)%, which indicates that the α-Sn film is fully epitaxially constrained to the InSb(111) in-plane lattice constant. The perpendicular strain from the experiment is $\varepsilon_{\perp}$ = (+0.006 ± 0.015)%, which is essentially zero within the experimental error.

Fig. 2a shows the calculated band structure of unstrained bulk α-Sn. Its CB and VB touch at the zone center, resulting in a single-point Fermi surface. The CB and VB nearby have quadratic dispersions; thus, the system is not a Dirac semimetal, but an ordinary or "Schrodinger" semimetal[2]. This particular band topology is protected by the cubic symmetry of the system, but can be readily modified by a uniaxial strain[26,29]. Note that the order of the Γ_8^+ CB and the Γ_7^- VB in α-Sn is inverted; modification to the band topology can lead to non-trivial topological phases[26,30]. The theoretical band structure of bulk α-Sn under the experimentally observed strain ($\varepsilon_{\parallel} = -0.14\%$) is shown in Fig. 2b for an overview and in Figs. 2c-d for a detailed view. The strain causes the CB and VB to move closer together, resulting in a small (negative) gap of Δ ~20 meV at the Γ point. As shown in Fig. 2g, the single-point Fermi surface in the unstrained case now splits into two points at (0, 0, $\pm k_D$), with $k_D = 0.017(2\pi/c)$. The system remains a semimetal. The dispersion

relations near the two contact points are linear in all three momentum directions; these features are indicative of a TDS. Given that the inverted band order in the unstrained system is preserved under strain, the 2D Z_2 index on the $k_z = 0$ plane is +1[30]. Following the usual classification criteria[13], strained α-Sn is indeed a TDS. The two bulk Dirac points, BDP1 and BDP2 as indicated in Fig. 2g are protected by the three-fold rotational symmetry in the strained structure, although the value of k_D depends on the strain (Supplementary Information A and B).

Evidently, this is the first report of a TDS phase in α-Sn. Prior studies have reported instead a TI phase under strain[26,29]. The differences can be attributed to either a different direction[26] or a different sign of the strain[29]. Fig. 2e shows a calculated bulk band structure of α-Sn with a positive strain of $\varepsilon_{\parallel} = 0.7\%$. An absolute gap of ~50 meV is obtained, and the system is a TI because of the band inversion. At an even larger $\varepsilon_{\parallel}$ of 1.5%, the system becomes an ordinary semimetal (OS) because of the band overlap, as shown in Fig. 2f. The phase diagram in Fig. 2h summarizes the systematics; the system is a TDS for a negative strain, becomes a Schrodinger semimetal at zero strain, transforms into a TI at positive strain and finally becomes an OS at a sufficiently large positive strain.

ARPES was employed to examine our negatively strained films. Fig. 3a shows a Fermi surface map of a 6-BL film. It is a single point at the zone center, which corresponds to the projection of the two bulk Dirac points of strained α-Sn. The in-plane band dispersion of the same film along $\bar{K}$-$\bar{\Gamma}$-$\bar{K}$ determined by ARPES mapping is shown in Fig. 3b. Right below the Fermi level E_F is a band that disperses linearly (red dashed lines) away from the single-point Fermi surface. The green lines indicate another valence band feature with linear band dispersion relations. For comparison, Fig. 3c shows calculated ARPES spectral functions deduced from the surface-projected density of states of a semi-infinite α-Sn slab. The major features agree well between theory and experiment. The red lines in Fig. 3b correspond to the top valence band. The green lines are associated with a Dirac point at about 0.3 eV binding energy; the relevant states have a strong surface character and originate from a topological surface band, but they become surface resonances because of the presence of degenerate bulk states.

In order to view the dispersion relations of the CB, which normally sits above the Fermi level, we use potassium (K) for electron doping of the surface[5,6]. Figs. 3d-e show a comparison of the electronic structure of a 6-BL α-Sn film before and after surface deposition of K, respectively. The net effect is a shift of the Fermi level upward by 0.21 eV, thus revealing part of the CB as a V-shaped band. The dispersion relations are shown again, with an enlarged scale, in Fig. 3f for comparison with the computed projection of the bulk bands onto the $k_z = 0$ plane as presented in Fig. 3g. Fig. 3h displays measured constant-energy contours at various binding energies. The contour is a circle at the high energy end, shrinks to a point at the Dirac point, and opens up into a circle again at lower energies; this latter circle is strongly modulated in intensity and appears more like two spots. The modulation can be attributed to matrix element effects associated with the s-polarization geometry in our experiments[31]. The weak CB feature in Fig. 3f can be enhanced by taking the second derivative of the data; the results are shown as an intensity map in Fig. 3i and as a set of momentum distribution curves in Fig. 3j. Curve fitting of the results yields peak positions as shown in Figs. 3j-k. It clearly shows a V-shaped CB with linear dispersions. The Fermi velocity along $\bar{\Gamma}\bar{K}$ of is 7.09 eV·Å or 1.07×10^6 m·s^{-1} for the CB and 2.16 eV·Å or 3.26×10^5 m·s^{-1} for the VB. These values are comparable to that of a high mobility TDS Cd_3As_2[6,7].

ARPES measurements of the bands have also been carried out with different photon energies to map out the band dispersion relations along k_z. Some of the key results obtained for 6-, 10- and 30-BL α-Sn films doped with K are shown in Fig. 4a. Corresponding computed band dispersion relations at various k_z are shown in Fig. 4b. The CB shifts to partly below the Fermi level by K doping. However, this energy shift is reduced as the film thickness increases because the electrons from K doping are diluted throughout the film thickness. As a result, the visible part of the CB is very much reduced for the 30-BL film. Evidently, the measured band dispersion relations for the 6- and 10-BL films do not change with photon energy, while the results for the 30-BL film show significant variations. This different behavior is highlighted in Fig. 4c, which plots the top of the VB at the zone center as a function of photon energy and film thickness. Thus, the 30-BL film is characterized

by 3D band dispersions with substantial variations along k_z, while the thinner films are characterized by 2D band dispersions.

Shown in Fig. 4b are computed in-plane band dispersion relations along k_x for bulk α-Sn at various values of k_z chosen to correspond closely to the 30-BL data in Fig. 4a. These k_z values are also consistent with the photon energies chosen for the experiment based on a free-electron final band dispersion[32]. When $k_z = k_D$ (42 eV photon energy), the calculated band structure shows a Dirac point with Λ-shaped linear dispersion relations for the VB, in agreement with experiment (See Supplementary Information C for details). As k_z moves away, a gap develops between the VB and CB. Fig. 4d shows the experimental and theoretical k_z dispersion relations of bulk α-Sn. The agreement is excellent. Note that band mapping along k_z is inherently limited by a finite momentum resolution due to a finite mean free path of the photoelectrons[32], and so the method does not permit a mapping of the details near $k_z = 0$. The experimental Λ-shaped linear dispersion for the VB at $k_z = k_D$ yields a Fermi velocity of 0.66 eV·Å or 1.0×10^5 ms^{-1}, which is much smaller than that for the in-plane dispersion.

The 2D character of the band dispersions for the 6- and 10-BL films can be understood as a result of quantum confinement[33]. The bulk bands are discretized into quantum well states or subbands characterized by subband indices that can be related to specific k_z values. The Dirac cones seen for the 6- and 10-BL films are 2D Dirac cones, similar to those observed in graphene[10] or the topological surface states in 3D topological insulators[11]. However, the Dirac cones in the Sn films are derived from 3D electronic states. The differences in the results between the 30-BL film and the thinner films indicate a transition or crossover from a 3D Dirac semimetal to a 2D Dirac semimetal.

Our results establish the first known case of a 3D TDS based on a simple elemental material. This finding is against the backdrop of a common impression that occurrences of 3D TDSs are limited to exotic materials with unusual chemical structures. Note that C (diamond), Si, Ge and α-Sn are isoelectronic and share the same crystal structure, but only α-Sn can be driven into a TDS phase by strain. This unique behavior is because the large spin-orbit

coupling in Sn leads to an inverted band ordering in the parent phase. The symmetry-required contact point between the CB and VB can transform into a positive or negative gap by the application of strain. Such topological transformations then lead to either a TI or a TDS, under a positive or negative strain, respectively. Prior studies explored only the positive strain side of the phase diagram. Thinner α-Sn films are 2D Dirac semimetals; the Dirac states are very similar to those seen in graphene, suggesting many possible applications based on existing graphene research. Our work indicates that α-Sn is a promising material for device applications based on its rich topological phase diagram.

Methods

Film growth and ARPES. The experiments were performed at the HERS endstation of Beamline 10.0.1, Advanced Light Source, Lawrence Berkeley National Laboratory. The substrates for film growth were InSb(111)-B wafers cleaned by repeated cycles of Ar^+ sputtering and annealing at 400 °C in an MBE chamber attached to the beamline. A sharp RHEED pattern characteristic of the 3×3 surface reconstruction of InSb(111)-B was observed after cleaning. Thin films of α-Sn were grown by evaporation of high-purity Sn from a Knudsen cell at a rate of ~3 minutes each bilayer onto a substrate kept at room temperature. Each sample after growth was transferred under vacuum to the ARPES chamber. Doping of the surface with K was performed with a SAES Getter dispenser. ARPES data were taken with a Scienta R4000 electron analyzer with the sample maintained at 40 K with liquid helium cooling. An *s*-polarization geometry was employed for the ARPES measurements. The overall energy and angular resolutions were 16 meV and 0.1°, respectively.

Strain measurements. After ARPES measurements, the 30-BL α-Sn film was taken out and transferred to Beamline 12.3.2, Advanced Light Source, for strain measurements by X-ray diffraction[34]. A grazing incidence geometry was employed to enhance the signal from the thin film sample. The X-ray beam from a superconducting wiggler source was focused down to a size of 1x1 μm^2 onto the sample using a pair of elliptically-bent

Kirkpatrick-Baez mirrors. The diffracted X-rays were detected with a DECTRIS Pilatus 1M hybrid pixel area detector placed at a diffraction angle of $2\theta = 90^{o}$. At first a Laue pattern from the sample was collected using polychromatic radiation to determine the orientation of the film and the exact angular positions of a number of reflections. Then, a monochromatized beam was employed to determine precisely the energy (wavelength) of each reflection, from which the *d*-spacings and thus the strain were extracted. The lattice parameter for unstrained bulk α-Sn used in strain computation was 6.4892 Å[35]. The $\sin^2\psi$ method[36] was used to determine the strain values parallel and perpendicular to the film. A silicon sample was used for calibrating the geometry and the monochromator.

Electronic structure calculations. The electronic structure of bulk α-Sn was computed using density functional theory (DFT) and Hartwigsen-Goedecker-Hutter (HGH) relativistic separable dual-space Gaussian pseudopotentials[37]. A plane-wave basis set was employed as implemented in the ABNIT package[38]. Spin-orbit coupling was taken into account. The cutoff of electron kinetic energy was 340 eV. A *k*-space gird of 12×12×8 was adopted based on the Monkhorst-Pack algorithm. The exchange-correlation functional was obtained with the modified Becke-Johnson Local Density Approximation (MBJLDA) method[39]. This method corrects a well-known problem that standard LDA calculations do not yield a correct conduction band edge of α-Sn at the *L* point[40] (Supplementary Information D). The lattice constant of bulk α-Sn was taken to be the experimental value $a = 6.4892$ Å[35]. When an in-plane strain of $\varepsilon_{\parallel}$ was applied to α-Sn, the perpendicular strain was taken to be $\varepsilon_{\perp} = -\varepsilon_{\parallel}/\sigma^{111}$, where σ^{111} is the Poisson's ratio of α-Sn along the [111] direction. Based on the elastic stiffness constants of α-Sn[41], $\sigma^{111} = \frac{c_{11}+2c_{12}+4c_{44}}{2c_{11}+4c_{12}-4c_{44}} = 2.467$. To calculate the electronic structure and surface-weighted charge density of semi-infinite α-Sn, we constructed a tight-binding model for the *s* and *p* orbitals of Sn. The interactions up to the third nearest neighbors as well as spin-orbit coupling were included in the model[40,42]. The tight-binding parameters were obtained by fitting HSE+SO calculations performed with the VASP package[43,44].

Acknowledgements

This work is supported by the U.S. Department of Energy (DOE), Office of Science (OS), Office of Basic Energy Sciences, Division of Materials Science and Engineering, under Grant No. DE-FG02-07ER46383 (T.C.C.) and DE-FG02-97ER45632 (M.Y.C.). The Advanced Light Source is supported by the Office of Basic Energy Sciences of the U.S. DOE under Contract No. DE-AC02-05CH11231. Y.H.C. is supported by a Thematic Project at Academia Sinica. X.X.W. is supported by the National Science Foundation of China under Grant No. 11204133. H. R. acknowledges support from Max Planck Korea/POSTECH Research Initiative of the NRF under Project No. NRF-2011-0031558.

Author contributions

C.Z.X. and T.C.C. conceived the work and planned the experiments. C.Z.X., with the aid of P.C., M.H.W., H.R., J.A.H., Z.H., S.K.M. and T.C.C., performed film growth and ARPES measurements and analyzed the data. C.D. and N.T. performed strain measurements and N.T. analyzed the resulting data. C.Z.X., Y.H.C., X.X.W. and M.Y.C. performed first-principles calculations. Y.C. and H.Y.K. provided additional theoretical support. C.Z.X., T.C.C. and S.K.M. wrote the paper. T.C.C. and S.K.M. jointly led the project.

1. Wan, X., Turner, A. M., Vishwanath, A. & Savrasov, S. Y. Topological semimetal and Fermi-arc surface states in the electronic structure of pyrochlore iridates. *Phys. Rev. B* **83,** 205101 (2011).
2. Young, S. M. *et al.* Dirac Semimetal in Three Dimensions. *Phys. Rev. Lett.* **108,** 140405 (2012).
3. Wang, Z. *et al.* Dirac semimetal and topological phase transitions in A_3Bi (A=Na, K, Rb). *Phys. Rev. B* **85,** 195320 (2012).
4. Wang, Z., Weng, H., Wu, Q., Dai, X. & Fang, Z. Three-dimensional Dirac semimetal and quantum transport in Cd_3As_2. *Phys. Rev. B* **88,** 125427 (2013).
5. Liu, Z. K. *et al.* Discovery of a Three-Dimensional Topological Dirac Semimetal, Na_3Bi. *Science* **343,** 864–867 (2014).
6. Liu, Z. K. *et al.* A stable three-dimensional topological Dirac semimetal Cd_3As_2. *Nat. Mater.* **13,** 677–681 (2014).
7. Neupane, M. *et al.* Observation of a three-dimensional topological Dirac semimetal phase in high-mobility Cd_3As_2. *Nat. Commun.* **5,** 3786 (2014).
8. Borisenko, S. *et al.* Experimental Realization of a Three-Dimensional Dirac Semimetal. *Phys. Rev. Lett.* **113,** 27603 (2014).
9. Xu, S.-Y. *et al.* Observation of Fermi arc surface states in a topological metal. *Science* **347,** 294–298 (2015).
10. Castro Neto, A. H., Guinea, F., Peres, N. M. R., Novoselov, K. S. & Geim, A. K. The electronic properties of graphene. *Rev. Mod. Phys.* **81,** 109–162 (2009).
11. Hasan, M. Z. & Kane, C. L. Colloquium : Topological insulators. *Rev. Mod. Phys.* **82,** 3045–3067 (2010).
12. Qi, X.-L. & Zhang, S.-C. Topological insulators and superconductors. *Rev. Mod. Phys.* **83,** 1057–1110 (2011).
13. Yang, B. & Nagaosa, N. Classification of stable three-dimensional Dirac semimetals with nontrivial topology. *Nat. Commun.* **5,** 4898 (2014).
14. Feng, J. *et al.* Large linear magnetoresistance in Dirac semi-metal Cd_3As_2 with Fermi surfaces close to the Dirac points. *Phys. Rev. B* **92,** 081306(R) (2014).
15. Narayanan, A. *et al.* Linear magnetoresistance caused by mobility fluctuations in n-Doped Cd_3As_2. *Phys. Rev. Lett.* **114,** 117201 (2015).
16. He, L. P. *et al.* Quantum Transport Evidence for the Three-Dimensional Dirac Semimetal Phase in Cd_3As_2. *Phys. Rev. Lett.* **113,** 246402 (2014).
17. Liang, T. *et al.* Ultrahigh mobility and giant magnetoresistance in the Dirac semimetal Cd_3As_2. *Nat. Mater.* **14,** 280–284 (2014).
18. Xiong, J. *et al.* Evidence for the chiral anomaly in the Dirac semimetal Na_3Bi. *Science* **350,** 413–416 (2015).
19. Li, C. *et al.* Giant negative magnetoresistance induced by the chiral anomaly in individual Cd_3As_2 nanowires. *Nat. Commun.* **6,** 10137 (2015).
20. Li, H. *et al.* Negative Magnetoresistance in Dirac Semimetal Cd_3As_2. *Nat. Commun.* **7,** 10301 (2015).
21. Moll, P. J. W. *et al.* Transport evidence for Fermi-arc-mediated chirality transfer in the Dirac semimetal Cd_3As_2. *Nature* **535,** 266–270 (2016).
22. Jeon, S. *et al.* Landau quantization and quasiparticle interference in the three-dimensional Dirac semimetal Cd_3As_2. *Nat. Mater.* **13,** 851–856 (2014).
23. Yi, H. *et al.* Evidence of topological surface state in three-dimensional Dirac

semimetal Cd_3As_2. *Sci. Rep.* **4,** 6106 (2014).
24. Osaka, T., Omi, H., Yamamoto, K. & Ohtake, A. Surface phase transition and interface interaction in the α-Sn/InSb{111} system. *Phys. Rev. B* **50,** 7567–7572 (1994).
25. Farrow, R. F. C. *et al.* The growth of metastable, heteroepitaxial films of α-Sn by metal beam epitaxy. *J. Cryst. Growth* **54,** 507–518 (1981).
26. Barfuss, A. *et al.* Elemental Topological Insulator with Tunable Fermi Level: Strained α-Sn on InSb(001). *Phys. Rev. Lett.* **111,** 157205 (2013).
27. Zhu, F. *et al.* Epitaxial growth of two-dimensional stanene. *Nat. Mater.* **14,** 1020–1025 (2015).
28. Xu, Y. *et al.* Large-Gap Quantum Spin Hall Insulators in Tin Films. *Phys. Rev. Lett.* **111,** 136804 (2013).
29. Roman, B. & Ewald, A. Stress-Induced Band Gap and Related Phenomena in Gray Tin. *Phys. Rev. B* **5,** 3914–3932 (1972).
30. Fu, L. & Kane, C. L. Topological insulators with inversion symmetry. *Phys. Rev. B* **76,** 45302 (2007).
31. Cao, Y. *et al.* Mapping the orbital wavefunction of the surface states in three-dimensional topological insulators. *Nat. Phys.* **9,** 499–504 (2013).
32. Chiang, T.-C., Knapp, J. A., Aono, M. & Eastman, D. E. Angle-resolved photoemission, valence-band dispersions $E(k)$, and electron and hole lifetimes for GaAs. *Phys. Rev. B* **21,** 3513–3522 (1980).
33. Chiang, T. C. Photoemission studies of quantum well states in thin films. *Surf. Sci. Rep.* **39,** 181–235 (2000).
34. Tamura, N. *et al.* A superbend X-ray microdiffraction beamline at the advanced light source. *Mater. Sci. Eng. A* **524,** 28–32 (2009).
35. Thewlis, J. & Davey, A. R. Thermal Expansion of Grey Tin. *Nature* **174,** 1011–1011 (1954).
36. Macherauch, E. & Muller, P. Das $\sin^2\psi$-Verfahren der röntgenographischen Spannungsmessung. *Zeitschrift für Angew. Phys.* **13,** 305–312 (1961).
37. Hartwigsen, C., Goedecker, S. & Hutter, J. Relativistic separable dual-space Gaussian pseudopotentials from H to Rn. *Phys. Rev. B* **58,** 3641 (1998).
38. Gonze, X. *et al.* ABINIT: First-principles approach to material and nanosystem properties. *Comput. Phys. Commun.* **180,** 2582–2615 (2009).
39. Tran, F. & Blaha, P. Accurate Band Gaps of Semiconductors and Insulators with a Semilocal Exchange-Correlation Potential. *Phys. Rev. Lett.* **102,** 226401 (2009).
40. Küfner, S., Fitzner, M. & Bechstedt, F. Topological α-Sn surface states versus film thickness and strain. *Phys. Rev. B* **90,** 125312 (2014).
41. Madelung, O. *Semiconductors: Group IV Elements and III-V Compounds*. (Springer-Verlag, Berlin, 1991).
42. Pedersen, T. G., Fisker, C. & Jensen, R. V. S. Tight-binding parameterization of α-Sn quasiparticle band structure. *J. Phys. Chem. Solids* **71,** 18–23 (2010).
43. Kresse, G. & Furthmüller, J. Efficiency of *ab-initio* total energy calculations for metals and semiconductors using a plane-wave basis set. *Comput. Mater. Sci.* **6,** 15–50 (1996).
44. Kresse, G. & Furthmüller, J. Efficient iterative schemes for *ab initio* total-energy calculations using a plane-wave basis set. *Phys. Rev. B* **54,** 11169–11186 (1996).

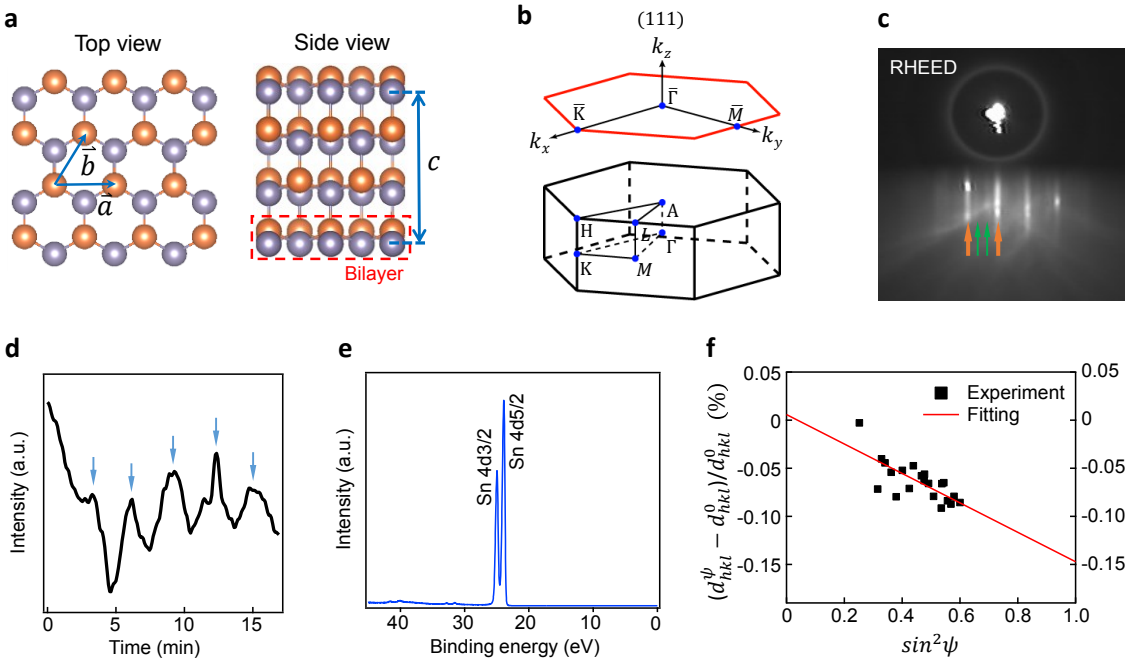

Figure 1 | Crystal structure, RHEED pattern and strain analysis of α-Sn films on InSb(111). **a**, Top and side views of the crystal structures of α-Sn films. The red dashed rectangle in side view shows the bilayer (BL) unit of α-Sn. **b**, Bulk Brillouin zone and (111)-projected surface Brillouin zone of α-Sn. **c**, A RHEED pattern of a 30-BL α-Sn film. The orange (green) arrows mark main (fractional) streaks. **d**, RHEED intensity as a function of growth time. The blue arrows mark when each BL is formed. **e**, A core-level photoemission spectrum for a 30-BL α-Sn film shows the characteristic Sn 4*d* doublet. **f**, Strain analysis of a 30-BL Sn film based on $sin^2\psi$ technique. d'_{hkl} (d^0_{hkl}) is the interplanar spacing for the (hkl) plane of the measured α-Sn film (unstrained α-Sn). ψ is the angle of each (hkl) plane with respect to the film surface plane.

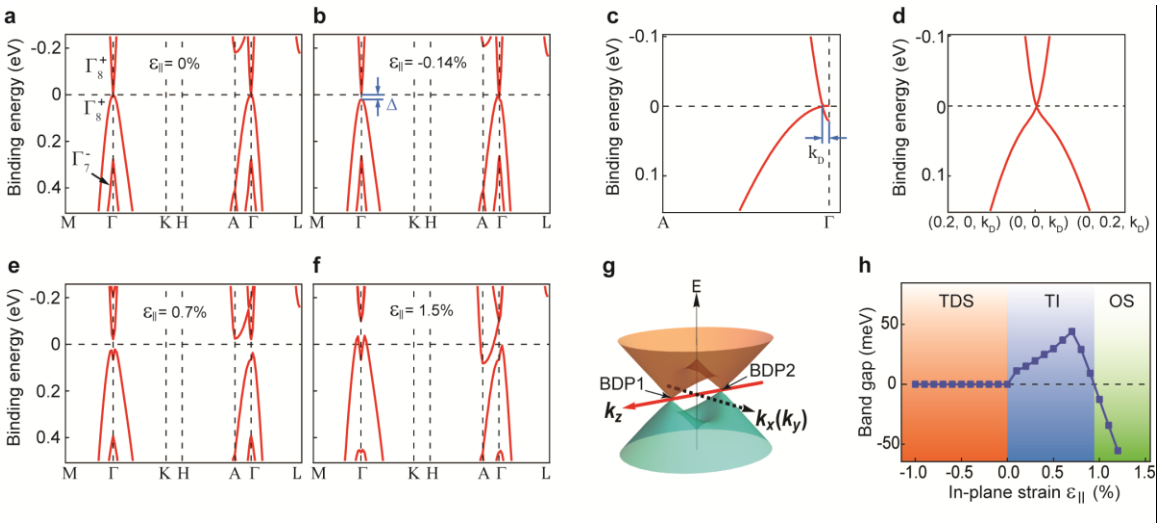

Figure 2 | Calculated electronic structure of α-Sn and its dependence on strain. a, Bulk band structure of α-Sn without strain. **b**, Bulk band structure of α-Sn with the same strain ($\varepsilon_{\parallel} = -0.14\%$) as that observed experimentally. **c**, Close-up view of **b** along the ΓA direction (k_z direction). The wave number of the band crossing point is $k_D = 0.017(2\pi/c)$. **d**, Bulk band structure of strained α-Sn along the k_x and k_y directions near the bulk Dirac point. **e**-**f**, Same as **b**, but with in-plane strain $\varepsilon_{\parallel}$ different in signs and magnitude as indicated. **g**, schematic illustration of the 3D TDS electronic structure of strained α-Sn. BDP1 and BDP2 marks the positions of two bulk Dirac points. **h**, Phase diagram and band gap of α-Sn as a function of in-plane strain $\varepsilon_{\parallel}$. The band gap is defined as $E_c - E_v$, where E_c (E_v) is the band edge of conduction (valence) band.

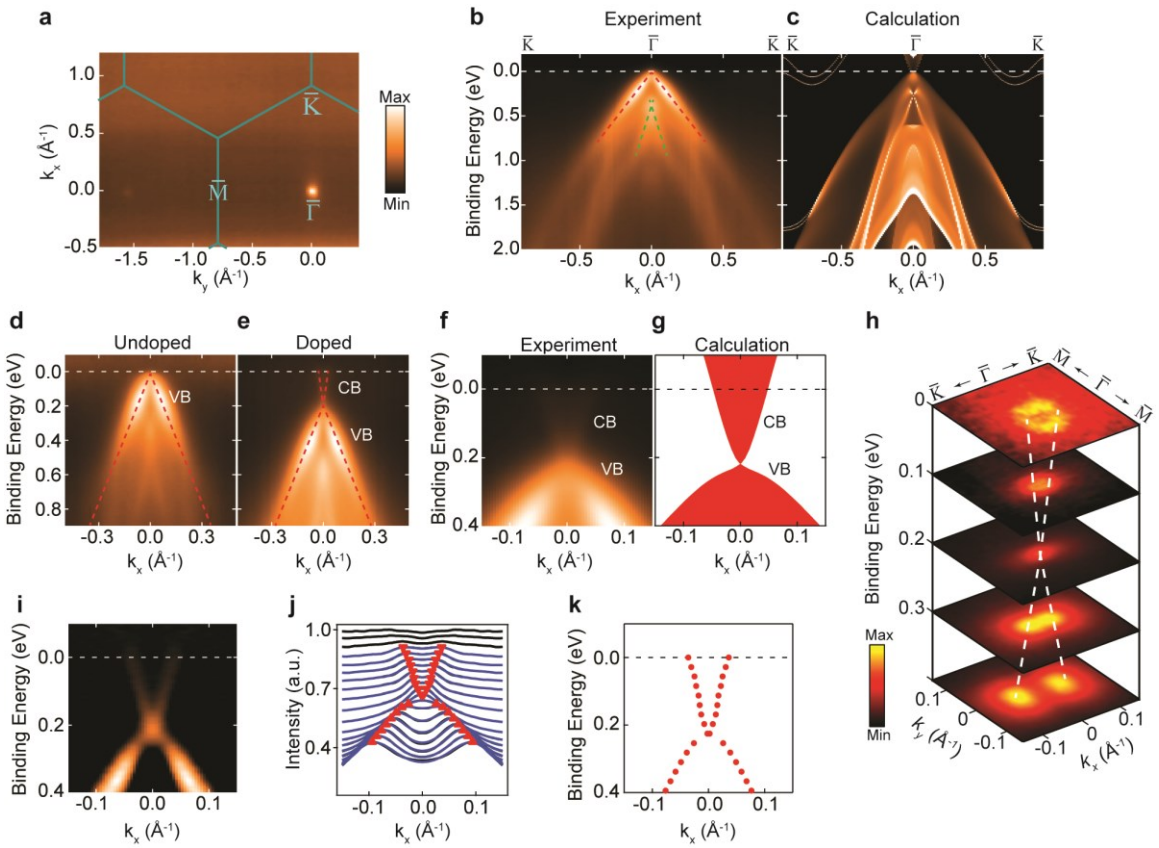

Figure 3 | Electronic structure of a 6-BL α-Sn film. a, Experimental Fermi surface. **b**, Experimental band dispersion along $\bar{K} - \bar{\Gamma} - \bar{K}$. **c**, Calculated ARPES spectral function of a semi-infinite α-Sn slab in the same scale as that in **b**. **d-e**, Band dispersion before and after *in situ* electron doping using a potassium metal dispenser, respectively. **f**, Close-up view of band dispersion in **e** around the zone center near the Fermi level. **g**, Calculated bulk bands projected onto (111) for comparison with **f**. **h**, Stacking plots of constant energy contours at different binding energies to show a Dirac cone. **i**, Second-derivative plot of experimental data shown in **f**. **j**, Momentum distribution curves obtained from experimental data in **f** (black curves) and peak fitting results (blue curves); these curves are essentially indistinguishable. Red triangles mark the peak positions for each blue curve. **k**, Peak positions from fitting results show a Dirac cone.

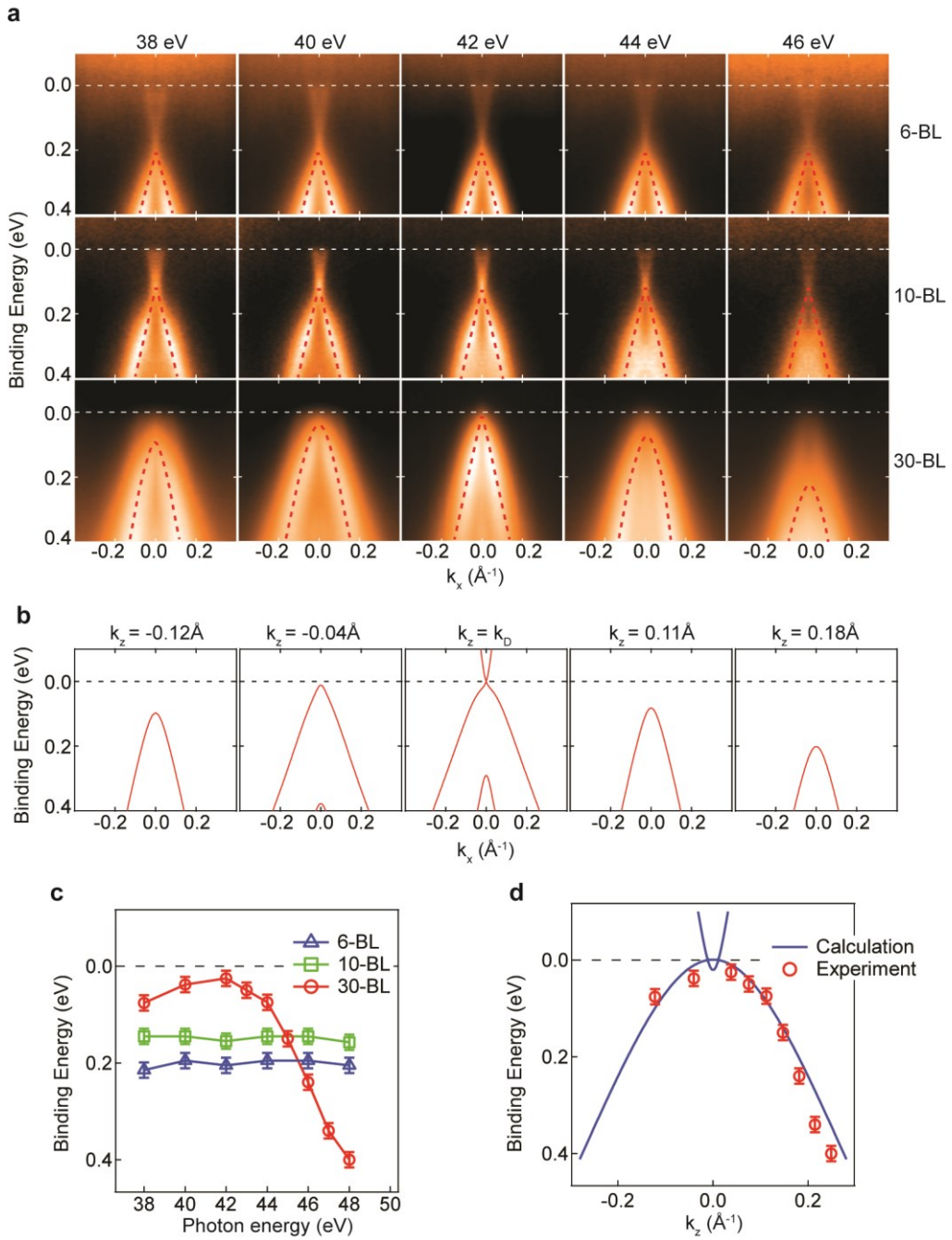

Figure 4 | Evolution of band dispersion of α-Sn films with film thickness and incident photon energy. **a**, ARPES maps from 6-, 10- and 30-BL α-Sn films under selected incident photon energies. **b**, Calculated band dispersions of bulk α-Sn along the k_x axis at various out-of-plane wave vector k_z. **c**, Evolution of the energy positon of the valence band top with incident photon energy for 6-, 10- and 30-BL α-Sn films. **d**, Band dispersions of a 30-BL α-Sn film along the out-of-plane direction (k_z) from experiment (circles) and theory (curves).